

1 **Soil organic carbon distribution for 0-3 m soils at 1 km²**
2 **scale of the frozen ground in the Third Pole Regions**

3
4 Dong Wang^{1,2}, Tonghua Wu^{1,3*}, Lin Zhao^{1,4}, Cuicui Mu⁵, Ren Li¹, Xianhua Wei⁶, Guojie
5 Hu¹, Defu Zou¹, Xiaofan Zhu¹, Jie Chen¹, Junmin Hao⁷, Jie Ni^{1,2}, Xiangfei Li^{1,2}, Wensi
6 Ma^{1,2}, Amin Wen^{1,2}, Chenpeng Shang^{1,2}, Yune La^{1,2}, Xin Ma^{1,2}, Xiaodong Wu¹

7
8 ¹ Cryosphere Research Station on the Qinghai-Tibetan Plateau, State Key Laboratory of
9 Cryospheric Science, Northwest Institute of Eco-Environment and Resource, Chinese
10 Academy of Sciences, Lanzhou, Gansu 730000, China

11 ² University of Chinese Academy Sciences, Beijing, 100049, China.

12 ³ Southern Marine Science and Engineering Guangdong Laboratory, Guangzhou 511458,
13 China.

14 ⁴ School of Geographical Sciences, Nanjing University of Information Science &
15 Technology, Nanjing 210000, China

16 ⁵ Key Laboratory of Western China's Environmental Systems (Ministry of Education),
17 College of Earth and Environmental Sciences, Lanzhou University, Lanzhou, 730000,
18 China.

19 ⁶ College of geography and environmental science, Northwest Normal University, Lanzhou
20 730070, China.

21 ⁷ School of civil engineering, Lanzhou University of Technology, Lanzhou, 730050, China.

22 *Correspondence: Tonghua Wu (thuawu@lzb.ac.cn)

23 **Abstract:** Soil organic carbon (SOC) is very important in the vulnerable ecological
24 environment of the Third Pole; however, data regarding the spatial distribution of SOC
25 are still scarce and uncertain. Based on multiple environmental variables and soil profile
26 data from 458 pits (depth of 0–1 m) and 114 cores (depth of 0–3 m), this study uses a
27 machine-learning approach to evaluate the SOC storage and spatial distribution at a
28 depth interval of 0–3 m in the frozen ground area of the Third Pole region. Our results
29 showed that SOC stocks (SOCS) exhibited a decreasing spatial pattern from the
30 southeast towards the northwest. The estimated SOC storage in the upper 3 m of the
31 soil profile was 46.18 Pg for an area of 3.27×10^6 km², which included 21.69 Pg and
32 24.49 Pg for areas of permafrost and seasonally frozen ground, respectively. Our results
33 provide information on the storage and patterns of SOCS at a 1 km² scale for areas of
34 frozen ground in the Third Pole region, thus providing a scientific basis for future
35 studies pertaining to Earth system models. The dataset is open-access and available at
36 <https://doi.org/10.5281/zenodo.4293454> (Wang et al., 2020).

37 **1 Introduction**

38 Soil is an important part of the global terrestrial ecosystem and represents the largest
39 terrestrial organic carbon pool with the longest turnover time (Amundson, 2001). This
40 is especially true in areas of frozen ground, including permafrost and seasonally frozen
41 ground. In cold environments, soil accumulates substantial organic carbon due to slow
42 decomposition rates and repeated freeze–thaw cycles (Fan et al., 2012; Li et al., 2020).
43 It has been reported that more than half of the world’s soil organic carbon (SOC) is
44 stored in permafrost regions (Hugelius et al., 2014; Ping et al., 2015). Even slight
45 changes in the decomposition of the SOC pool in permafrost regions might lead to
46 significant changes in the atmospheric CO₂ concentration, which plays an important
47 role in regulating and stabilizing the carbon balance of global ecosystems (Schuur et
48 al., 2015). Therefore, it is of great significance to accurately estimate the storage and
49 spatial distribution of SOC in regions of frozen ground in order to study the carbon
50 cycle of this ecosystem as well as global change.

51 As the “roof of the world”, the Third Pole is the area of frozen ground at the highest

52 average altitude in the middle and low latitudes of the Northern Hemisphere. The Third
53 Pole is also one of the most sensitive areas with respect to global climate change, and
54 has a warming rate that is approximately twice the global average (Stocker et al., 2013).
55 In the past few decades, permafrost in the Third Pole region has experienced obvious
56 degradation (Mu et al., 2020; Ran et al., 2017; Turetsky et al., 2019; Wu et al., 2012).
57 Permafrost degradation will not only cause serious geological disasters and affect
58 engineering construction in cold areas, but will also accelerate the decomposition of the
59 huge SOC pool stored in permafrost (Cheng et al., 2007; Cheng et al., 2019; Ding et al.,
60 2021). Moreover, it will emit a large amount of greenhouse gases into the atmosphere,
61 thus increasing the rate of climate change in the future (Schuur et al., 2015). Therefore,
62 accurate estimates of the SOC storage and spatial distribution in the areas of frozen
63 ground in the Third Pole region have become important for Earth system modeling.
64 Such estimates are widely used to study the carbon cycle of this ecosystem and global
65 change (Koven et al., 2011; Lombardozzi et al., 2016; McGuire et al., 2018).

66 Early studies were mostly based on data from China's national soil survey, and were
67 combined with regional vegetation/soil maps to estimate the SOC pool for a certain
68 vegetation type or relatively small area (Wang et al., 2002; Zeng et al., 2004). Up until
69 2008, the Chinese part of the Qinghai-Tibet Plateau (QTP) was taken as an independent
70 geographical unit to estimate the SOC pool in the upper 100 cm of the soil profile (Tian
71 et al., 2008; Wu et al., 2008). However, these studies did not distinguish between
72 regions of permafrost and seasonally frozen ground. In recent years, based on soil
73 profile data and vegetation/soil maps, some studies have estimated the SOC pool in the
74 QTP permafrost region (Mu et al., 2015; Zhao et al., 2018; Jiang et al., 2019). The
75 aforementioned studies improved our understanding of SOC storage in the Third Pole
76 region, but estimation results of 0-3m SOC pool have large uncertainties, ranging from
77 17.1 Pg to 40.9 Pg. In addition, the large-scale maps of vegetation and soil types used
78 in these studies were associated with large uncertainties because they were created years
79 ago and have a low spatial resolution, thus leading to potentially large errors in the
80 estimated total SOC pools (Mishra et al., 2013; Mu et al., 2020). Recently, considerable
81 progress has been made in digital soil mapping methods. Spatial interpolation, linear

82 regression, and machine learning have been widely used to simulate the spatial
83 distribution of SOC in the permafrost region of the QTP (Ding et al., 2016; Ding et al.,
84 2019; Wang et al., 2020; Yang et al., 2008). These studies have provided new spatial
85 data and improved the prediction accuracy of SOC compared with earlier studies.
86 However, few studies to date have systematically assessed SOC pools across areas of
87 seasonally frozen ground in the Third Pole region, which limits many investigations
88 requiring SOC data for these areas.

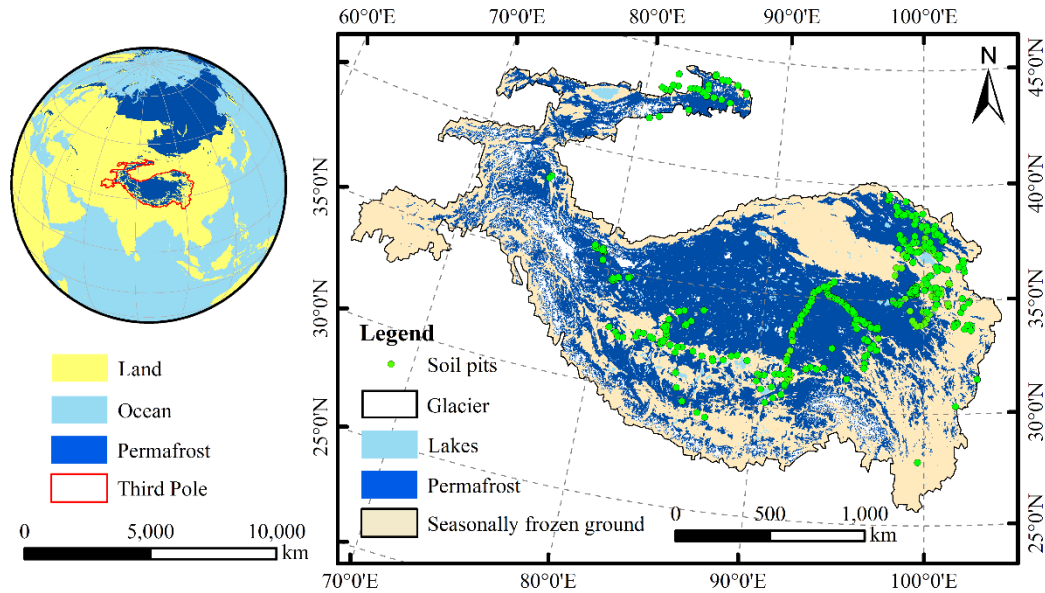
89 To evaluate the size and high-resolution spatial patterns of SOC stocks in the Third
90 Pole region, we carried out a large-scale field-sampling plan that covered representative
91 permafrost zones over the region's bioclimatic gradient, including a large unpopulated
92 area with harsh natural conditions. A total of 200 soil pits were excavated, most of
93 which were deeper than 2 m. In addition, we collected field-measured SOCS data for
94 the Third Pole region from relevant literature published between 2000 and 2016 (Ding
95 et al., 2016; Song et al., 2016; Xu et al., 2019; Yang et al., 2008). By combining high-
96 resolution remotely sensed data and interpolated meteorological datasets, we simulated
97 the spatial distribution of SOCS in the Third Pole region by three machine learning
98 methods and calculated the SOC storage of specific soil intervals (0–30 cm, 0–50 cm,
99 0–100 cm, 0–200 cm, and 0–300 cm). The results provide basic data for Earth system
100 modeling, and reference methods for studying the spatial distribution of soil elements
101 under complex terrain.

102 **2 Materials and Methods**

103 **2.1 Study area**

104 The Third Pole is the highest plateau in the world, and is located on the QTP and its
105 surrounding mountains, which include Pamir and Hindu Kush mountain ranges in the
106 west, the Hengduan Mountains in the east, the Kunlun and Qilian mountains in the
107 north, and the Himalayas in the south (Yao et al., 2012). In addition, the Third Pole is
108 the largest high-altitude permafrost zone in the Northern Hemisphere, with a total
109 permafrost area of approximately 1.72×10^6 km², thus representing ~8% of permafrost
110 regions in the Northern Hemisphere (Obu et al., 2019). The area of seasonally frozen
111 ground covers an area of approximately 1.55×10^6 km², which is mainly located in the

112 eastern and southern parts of the Third Pole as well as at lower elevations of basins
113 (Fig.1). Third Pole is mainly covered by five types of vegetation: forests, shrubs,
114 grasslands, croplands, and deserts (Hao et al., 2017).



115
116 **Figure 1.** Distribution of soil pits in the Third Pole region (the frozen ground map is derived from
117 Obu et al., 2019).

118 2.2 Data Processing

119 2.2.1 Soil organic carbon data

120 The collected SOC data used in this study included field investigated data and
121 available published data for total 371 soil sample (458 samples for the 0–100 cm soil
122 layer, and 113 samples for the 0–300 cm soil layer).

123 (1) Field measured data: a total of 200 soil pits were excavated between 2009 and
124 2011; 72 soil pits were excavated manually in 2009, and 128 soil pits were excavated
125 with hydraulic excavators in 2010 and 2011. Most of the pits were deeper than 2m,
126 unless rock layers were detected. For each soil profile, we collected soil samples at
127 depth intervals of 0–10 cm, 10–20 cm, 20–30 cm, 30–50 cm, 50–100, and 100–200 cm
128 (Fig. 2).

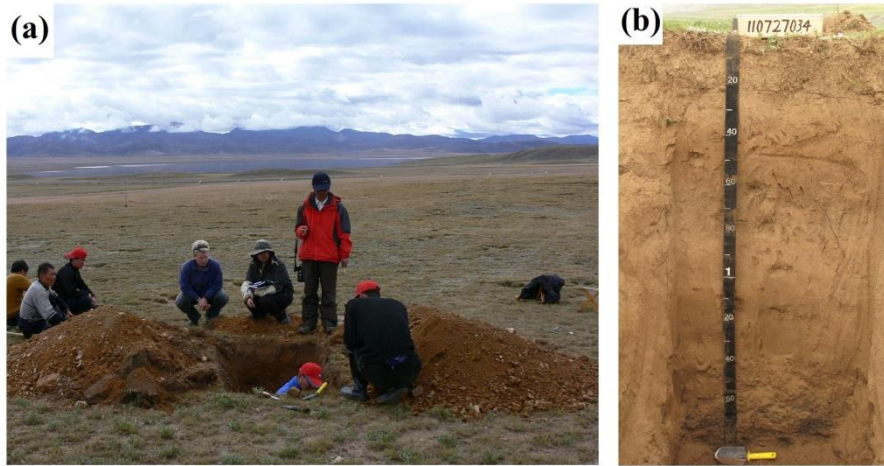


Figure 2. Field work photographs showing (a) soil sample collection, and (b) a soil profile.

The bulk density samples were obtained for each layer using a standard soil sampler (5 cm diameter and 5-cm-high stainless-steel cutting ring), and bulk density was calculated as the ratio of the oven-dry soil mass to the container volume. Soil samples for carbon analysis were air-dried, handpicked to remove plant detritus, and then sieved through a 2mm mesh to calculate the volume percentage of the gravel. The SOC content was determined using the Walkley-black method after soil samples were pretreated by air drying, grinding, and screening. The analyses were carried out in triplicate using subsamples, and the mean of three values was used as the SOC content. The SOCS was calculated using Eq. (1):

$$SOCS = \sum_{i=1}^n T_i \times BD_i \times SOC_i \times \frac{(1 - C_i)}{10} \quad (1)$$

where T_i , BD_i , SOC_i , and C_i are soil thickness (cm), dried bulk density ($\text{g}\cdot\text{cm}^{-3}$), SOC content (%) and > 2mm rock fragment content (%) at layer i .

(2) Available published data: we compiled all available information from the studies on SOC stocks in third pole regions published after 2000. The following 3 criteria are used to screen the data of SOC stocks from the published literature: (1) The SOC data must be field investigated data; (2) Eliminate sample data with missing geographic location information and sampling time; (3) SOC measuring methods were similar as our experimental procedure. Finally, the 4 papers selected encompassed the main ecosystems in Third Pole, namely forest, grassland, desert, cropland, and shrub ecosystems. Specifically, data pertaining to a soil depth interval of 0–30 cm ($n = 135$)

151 was retrieved from Yang et al. (2010) for the SOC database; data pertaining to a depth
 152 interval of 0–100 cm (n = 93) was obtained from Xu et al. (2019), data pertaining to a
 153 depth interval of 0–100 cm (n = 30) retrieved from Song et al. (2016). Moreover,
 154 additional data for 0–3 m and 0–2 m depth intervals (n = 113) were retrieved from Ding
 155 et al. (2016).

156 **Table 1** Summary of soil organic carbon datasets used in this study

Number of samples	Depth interval	Period	Method	Source
135	0–100 cm	2001–2005	Walkley-black method	Yang et al., 2010
30	Genetic horizon	2012–2013	Walkley-black method	Song et al., 2016
93	0–100 cm	2004–2014	Walkley-black method	Xu et al., 2019
113	0–200 cm and 0–300 cm	2013–2014	Walkley-black method	Ding et al., 2016
200	0–200 cm	2009–2013	Walkley-black method	Field-investigated

157 Combined with the available published data and field investigated data (Table 1), the
 158 458 soil pits (depth of 0–1 m) and 114 soil cores (depth of 0–3 m) can represent the
 159 vegetation types and characters in large areas of the Third pole (Table 2).

160 **Table 2** Number of soil sample points of different vegetation types in Third pole region

Vegetation types	Forest	Shrub	Grassland	Desert	Cropland
Number	10	22	371	49	6

161 2.2.2 Environmental Covariates

162 The environmental covariates used in this study included a digital elevation model
 163 (DEM), remotely sensed data, and spatial interpolation data (Table S1).

164 A DEM at a spatial resolution of 1 km × 1 km was downloaded from the International
 165 Scientific Data Service Platform (<http://datamirror.csdb.cn>). Using the DEM data and
 166 SAGA GIS software, we calculated 14 terrain attributes: elevation (H), slope (S), aspect
 167 (A), plan curvature (PlanC), profile curvature (ProC), topographic wetness index (TWI),
 168 total catchment area (TCA), relative slope position (RSP), slope length and steepness
 169 factor (LS), convergence index (CI), channel network base level (CNB), channel
 170 network distance (CND), valley depth (VD), and closed depressions (CD).

171 Mean annual air temperature (MAT) and mean annual precipitation (MAP) data were
172 downloaded from WorldClim version 2.1 (<https://www.worldclim.org>). These datasets
173 were generated by organizing, calculating, and spatially interpolating observed data
174 from global meteorological stations for the period 1970–2000.

175 Normalized difference vegetation index (NDVI) data were obtained from the United
176 States Geological Survey (USGS) (<http://modis.gsfc.nasa.gov/>). The datasets
177 underwent atmospheric, radiometric, and geometric correction, with a spatial resolution
178 of 1 km × 1 km for every 1-month interval over the period 2000–2015. The NDVI
179 product was calculated using the maximum value composite (MVC) method, which can
180 minimize the effects of aerosols and clouds (Stow et al., 2004).

181 The net primary productivity (NPP) and leaf area index (LAI) data were obtained
182 from the Global Land Surface Satellite (GLASS, V3.1), which is estimated from the
183 MODIS reflectance data using the general regression neural network (GRNN) method
184 (Liang et al., 2013). Data were at a 1 km resolution for 8 day periods between 2000 and
185 2015, and were downloaded from the National Earth System Science Data Center of
186 the National Science & Technology Infrastructure of China (<http://www.geodata.cn>).

187 The soil texture data, including sand, silt, and clay contents, were obtained from the
188 “SoilGrids250m database” (<http://www.isric.org>). The original 250 m spatial resolution
189 data were resampled to a 1 km resolution based on nearest neighbor interpolation using
190 ArcGIS 10.2 software (ESRI, Redlands, CA, USA).

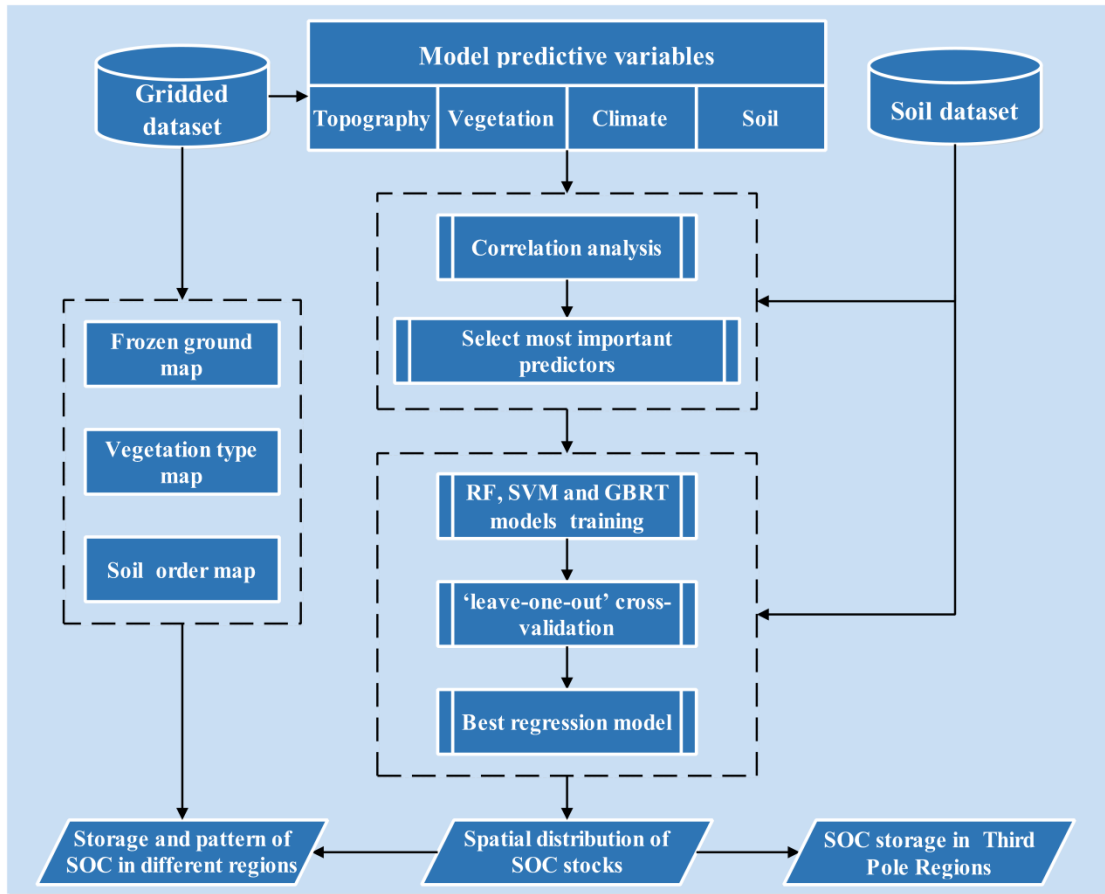
191 The land cover data used in this study were collected from the Land Cover Type
192 Climate Modeling Grid (CMG) product (MCD12C1) from 2010
193 (<https://lpdaac.usgs.gov>). The classification schemes in this study were based on the
194 global vegetation classification scheme of the International Geosphere Biosphere
195 Programme (IGBP). We reclassified the land cover types into five major categories:
196 forest, shrub, grassland, cropland, and desert.

197 **2.3 Model predictions**

198 **2.3.1. Geographical modelling and selection of the predictors**

199 In this study, three machine learning methods (random forest (RF), gradient boosted
200 regression tree (GBRT), and support vector machine (SVM)) were constructed and

201 validated using the SOCS in the upper 30 cm of soil profiles along with associated
 202 variables (Fig.3).



203
 204 **Figure 3.** Workflow diagram for predicting SOCSs in this study. RF: random forest; SVM:
 205 support vector machine; GBRT: gradient boosted regression tree.

206 With respect to the machine learning methods used, RF is used for classification,
 207 regression, and other tasks. It is operated by constructing a large number of decision
 208 trees during training, and outputs the class as the classification or regression patterns of
 209 single trees (Tin Kam, 1998). The GBRT method is an iterative fitting algorithm
 210 composed of multiple regression trees, and combines regression trees with a boosting
 211 technique to improve predictive accuracy (Elith et al., 2008). The SVM regression
 212 method uses kernel functions to construct an optimal hyperplane, which has a minimal
 213 total deviation (Drake and Guisan, 2006). Combined with the remotely sensed data and
 214 spatial interpolation data, RF, GBRT, and SVM regression were conducted to predict
 215 the SOCS in the Third Pole region. The ‘randomForest’, ‘gbm’, and ‘e1071’ packages
 216 in R were used to perform RF, GBRT, and SVM analyses.

217 The 15 input variables (H, S, TWI, TCA, RSP, CNB, CND, VD, NDVI, NPP, LAI,
 218 MAP, MAT, sand, and silt) for the three regression models were selected because they
 219 can reflect the effects of topography, climate, vegetation, and soil properties on regional
 220 SOCS. Moreover, these variables were significantly associated with the SOCS at a
 221 depth interval of 0–30 cm ($P < 0.01$, Table S2), whereas other environmental factors
 222 were eliminated due to their low correlation coefficients.

223 2.3.2 Estimation method of SOCS in deep soils

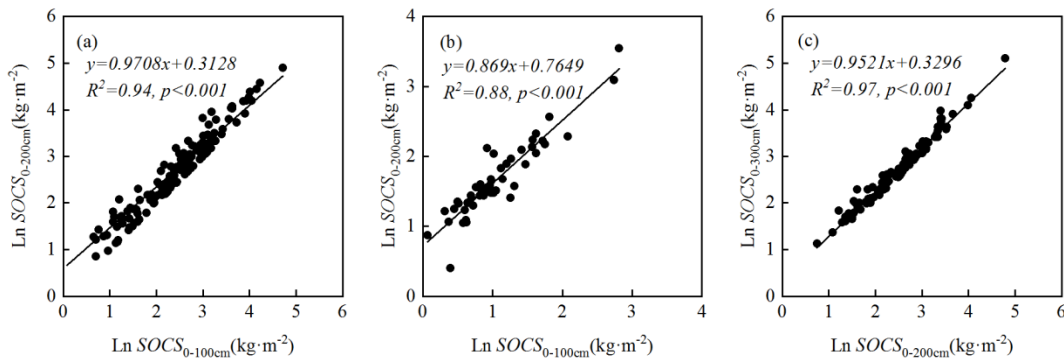
224 To generate the spatial distributions of SOCS in deep layers (below a depth of 100
 225 cm), we established nonlinear extrapolation models (Fig. 4.a–b; Eqs. (2)–(4)) between
 226 the SOCS in the upper 100 cm interval and the SOCS in the upper 200 cm interval using
 227 the data from the 200 soil pits in grassland ($n = 151$) and desert ecosystems ($n = 49$,
 228 Fig. S1). A third extrapolation model between the SOCS in the upper 200 cm interval
 229 and the SOCS in the upper 300 cm interval in grassland ecosystems was established
 230 using the data from 114 sites reported by Ding et al. (2016) (Fig 4.c; Eq. (4)).

$$231 \quad \ln SOCS_{0-200\text{cm}} = 0.9708 \times \ln SOCS_{0-100\text{cm}} + 0.3128 \quad (2)$$

$$232 \quad \ln SOCS_{0-200\text{cm}} = 0.8690 \times \ln SOCS_{0-100\text{cm}} + 0.7649 \quad (3)$$

$$233 \quad \ln SOCS_{0-300\text{cm}} = 0.9521 \times \ln SOCS_{0-200\text{cm}} + 0.3296 \quad (4)$$

234 where $\ln SOCS_{0-100\text{cm}}$, $\ln SOCS_{0-200\text{cm}}$ and $\ln SOCS_{0-300\text{cm}}$ are the natural logarithms of the
 235 soil organic carbon stocks ($\text{kg} \cdot \text{m}^{-2}$) at the depth intervals of 0–100 cm, 0–200 cm, and
 236 0–300 cm, respectively.



237

238 **Figure 4.** Extrapolation function of the SOCS between soil depth intervals of (a) 0–100 cm and 0–
 239 200 cm in grassland ecosystems, (b) 0–100 cm and 0–200 cm in desert ecosystems, and (c) 0–200

240 cm and 0–300 cm in grassland ecosystems

241 It is impossible to build extrapolation models directly to estimate deep SOC storage
242 in forest, shrub, and cropland ecosystems, which lack deep soil pits below 100 cm.
243 Therefore, according to the vertical distribution of the SOCS associated with different
244 land cover types worldwide from Jobbagy and Jackson (2000), the extrapolation models
245 shown in Eqs. (5)–(6) were established indirectly to estimate deep SOC storage (below
246 a depth of 100 cm) in areas of these land cover types (Fig. S1). Correspondingly, Eq.
247 (7) was established to estimate the deep SOC storage (below a depth of 200 cm) in
248 desert ecosystems due to a lack of deep soil pits below 200 cm.

$$249 \quad SOCS_{0-200cm} = (1 + \beta_{100-200cm}) \times SOCS_{0-100cm} \quad (5)$$

$$250 \quad SOCS_{0-300cm} = (1 + \beta_{100-200cm} + \beta_{200-300cm}) \times SOCS_{0-100cm} \quad (6)$$

$$251 \quad SOCS_{0-300cm} = SOCS_{0-200cm} + \beta_{200-300cm} \times SOCS_{0-100cm} \quad (7)$$

252 where $\beta_{100-200cm}$ and $\beta_{200-300cm}$ are proportion of $SOCS_{100-200cm}$ and $SOCS_{200-300cm}$ in
253 $SOCS_{0-100cm}$, respectively.

254 The calculation of the SOC storage (Pg) for a region generally uses Eq. (8):

$$255 \quad SOC_{storage} = \sum_{i=1}^n SOCS_i \times A \times 10^{-12} \quad (8)$$

256 where $SOCS_i$ is the SOCS ($\text{kg} \cdot \text{m}^{-2}$) at site i and A is the area (m^2) of each grid unit.

257 2.3.3 Model validation

258 To test the predictive effects of the three machine learning methods, “leave-one-out”
259 cross-validation was conducted. We used the R^2 value, the mean error (ME , Eq. (9)),
260 and the root mean square error ($RMSE$, Eq. (10)) to evaluate the performance of the
261 prediction models.

$$262 \quad ME = \frac{1}{n} \sum_{i=1}^n [D(x_i) - D^*(x_i)] \quad (9)$$

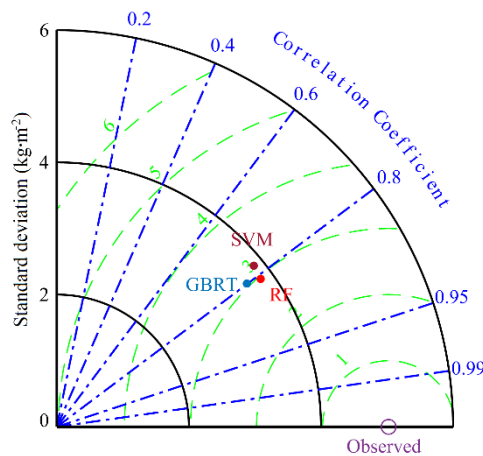
$$263 \quad RMSE = \sqrt{\frac{1}{n} \sum_{i=1}^n [D(x_i) - D^*(x_i)]^2} \quad (10)$$

264 where $D(x_i)$ is the measured SOCS, $D^*(x_i)$ is the predicted SOCS, and n is the number
265 of validation sites.

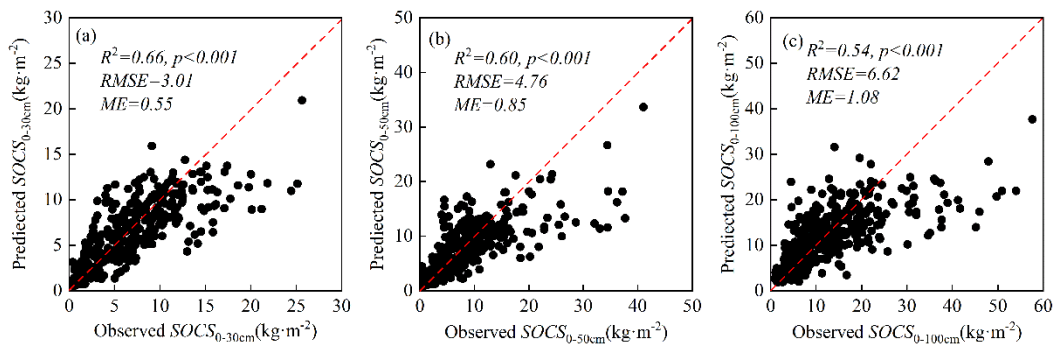
266 3 Results

267 **3.1 Performance of machine learning methods**

268 The results of the “leave-one-out” cross-validation showed that the RF model
 269 exhibited a Pearson’s correlation coefficient of 0.81, which was higher than that of the
 270 GBRT model (0.79) and SVM model (0.77). In addition, the *RMSE* of the RF model
 271 ($3.01 \text{ kg}\cdot\text{m}^{-2}$) was lower than that of the GBRT model ($3.11 \text{ kg}\cdot\text{m}^{-2}$) and SVM model
 272 ($3.21 \text{ kg}\cdot\text{m}^{-2}$) for the upper 30 cm of the soil profile (Fig. 5). These results suggest that
 273 the RF model provides a better tool for predicting the spatial distribution of SOCS in
 274 the Third Pole region. Moreover, in order to further discuss the simulation accuracy of
 275 the RF model in this study, “leave-one-out” cross-validations were conducted for depth
 276 intervals of 0–50 cm and 0–100 cm. The results revealed high R^2 as well as low *RMSE*
 277 and *ME* values (Fig. 6).



278
 279 **Figure 5.** A Taylor diagram used to evaluate the model performance of random forest (RF),
 280 support vector machine (SVM), and gradient boosting regression tree (GBRT) models, which
 281 were used to predict the SOCS in the upper 30 cm of soil profiles across the Third Pole. The
 282 contour centered on the observed indicates the root-mean-square error (*RMSE*, $\text{kg}\cdot\text{m}^{-2}$) between
 283 the predicted value and observed value.



284
 285 **Figure 6.** “Leave-one-out” cross-validation for the RF model used to predict the SOCS at (a) 0–30

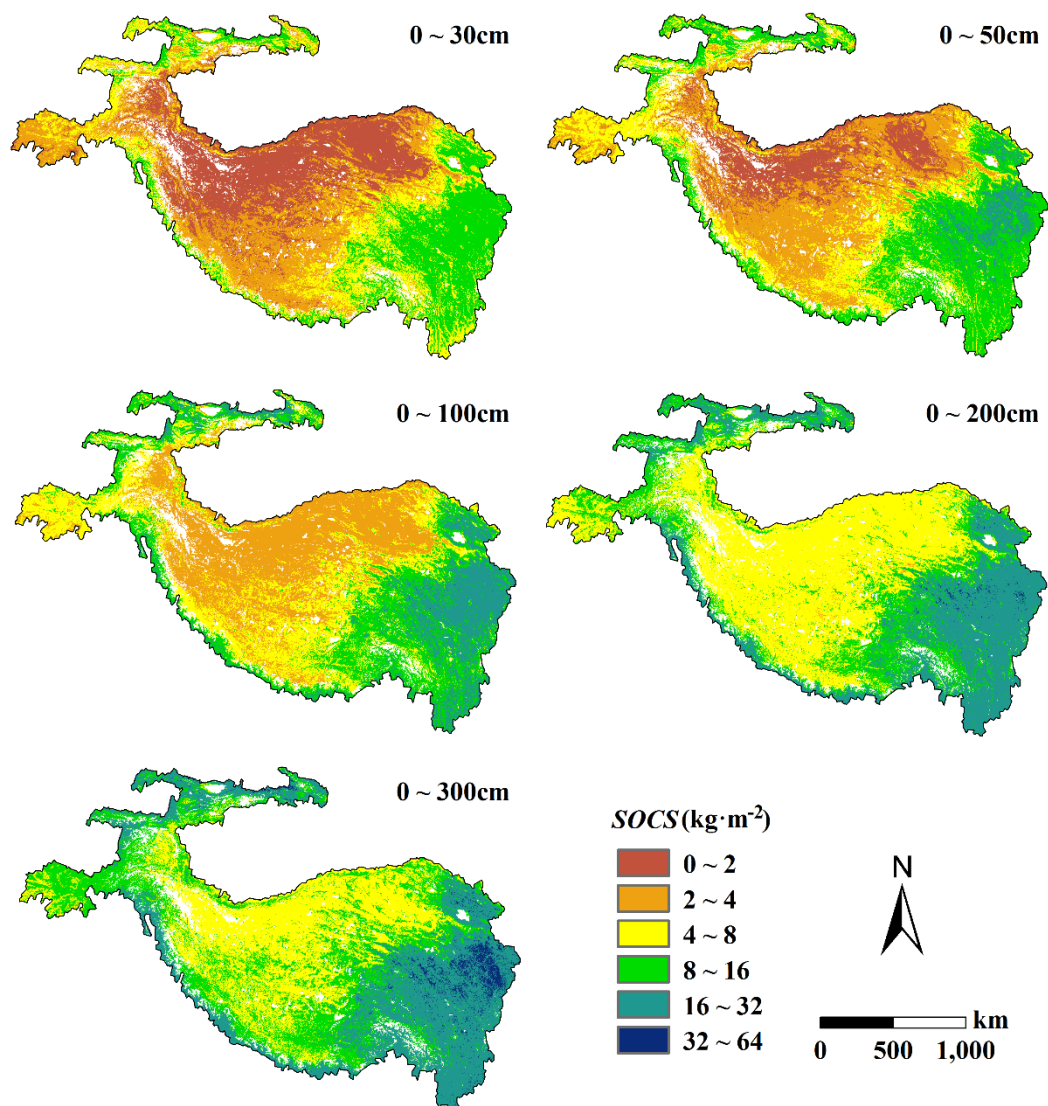
cm, (b) 0–50 cm, and (c) 0–100 cm depth intervals.

286

287

288 **3.2 Storage and spatial distribution of soil organic carbon**

289 Figure 7 shows a large spatial variability of the SOCS across the Third Pole region,
290 whereby an overall decreasing trend can be observed from the southeast towards the
291 northwest. The wetland area in the eastern region of the Third Pole (Ruoergai) had the
292 highest predicted SOCS for a depth interval of 0–300 cm ($> 32 \text{ kg}\cdot\text{m}^{-2}$), whereas the
293 northern region (Qiangtang Plateau and Qaidam Basin) had the lowest SOCS ($< 8 \text{ kg}\cdot\text{m}^{-2}$).
294 The estimated mean SOCS for the entire Third Pole region at depth intervals of 0–
295 30 cm, 0–50 cm, 0–100 cm, 0–200 cm, and 0–300 cm was $4.84 \text{ kg}\cdot\text{m}^{-2}$, $6.45 \text{ kg}\cdot\text{m}^{-2}$,
296 $8.51 \text{ kg}\cdot\text{m}^{-2}$, $11.57 \text{ kg}\cdot\text{m}^{-2}$, and $14.17 \text{ kg}\cdot\text{m}^{-2}$, respectively. Correspondingly, the total
297 estimated SOC storage was 15.79 Pg, 21.04 Pg, 27.75 Pg, 37.71 Pg, and 46.18 Pg at 0–
298 30 cm, 0–50 cm, 0–100 cm, 0–200 cm, and 0–300 cm, respectively (Table 3). In
299 addition, the SOCS decreased with increasing soil depth across the Third Pole region,
300 with 34.26% of the total SOC storage for a depth interval of 0–300 cm being contained
301 in the uppermost 30 cm, and only 17.89% in the 200–300 cm depth interval.



302

303 **Figure 7.** Spatial distribution of SOCS at different depth intervals over the Third Pole region.

304 Compared with the area of seasonally frozen ground, the mean SOCS and total SOC
 305 storage in the permafrost region were lower in each soil layer. The estimated amount of
 306 SOC stored at a depth interval of 0–300 cm in the permafrost and seasonal frozen
 307 ground zone were 21.69 Pg and 24.49 Pg, respectively, which accounted for 46.97%
 308 and 53.03% of the total SOC pools, respectively.

309

310

311

312

313

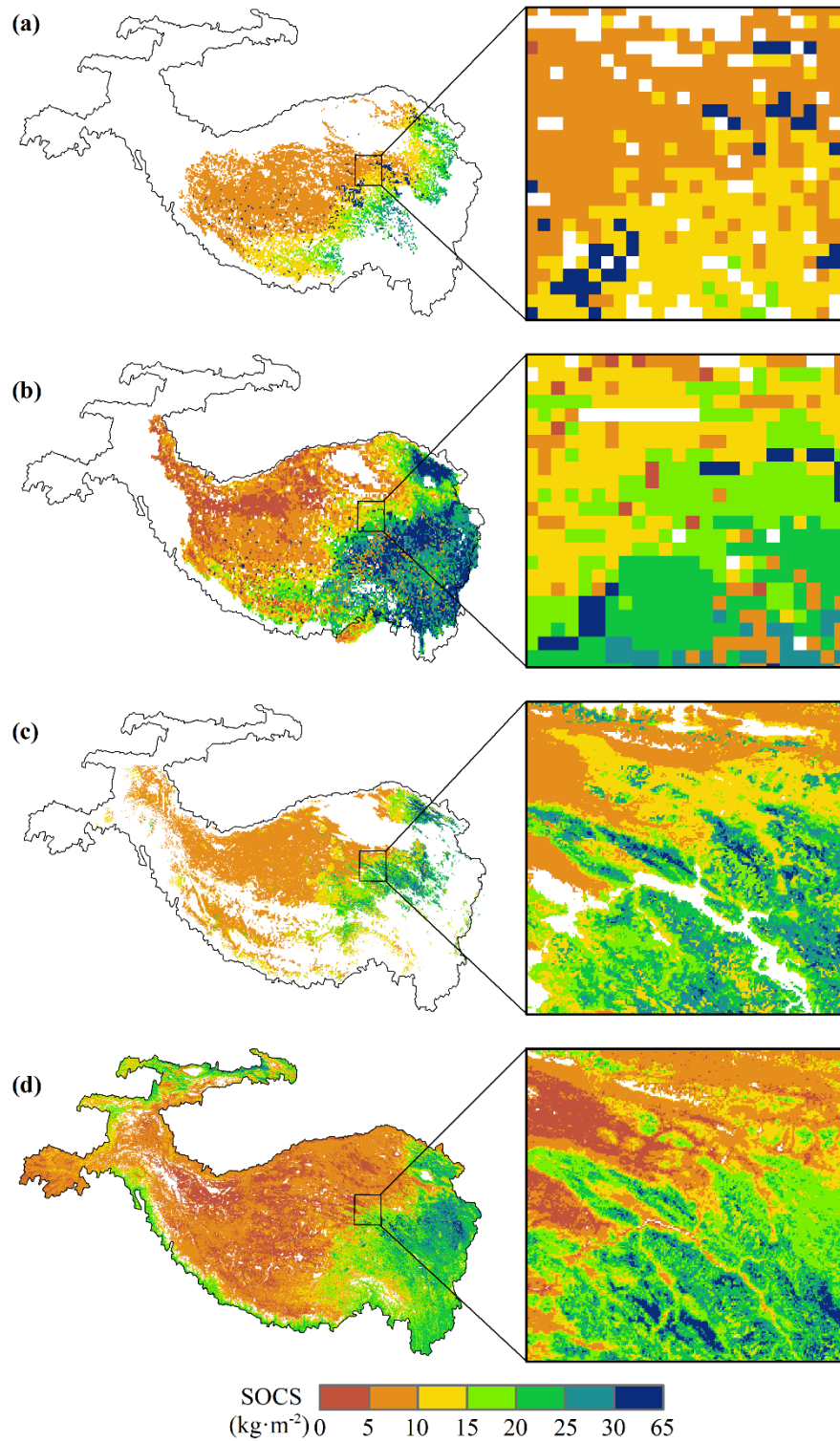
314 **Table 3** Summary of the estimated mean SOC stocks and storages in permafrost and seasonally
 315 frozen ground of the Third Pole

Depth (cm)	SOC stock ($\text{kg}\cdot\text{m}^{-2}$)			SOC storage (Pg)		
	Permafrost	Seasonally frozen ground	Third Pole	Permafrost	Seasonally frozen ground	Third Pole
0–30	4.13	5.56	4.84	7.61	8.63	15.79
0–50	5.72	7.16	6.45	10.53	11.12	21.04
0–100	7.28	9.70	8.51	13.41	15.06	27.75
0–200	10.25	12.88	11.57	18.88	19.99	37.71
0–300	12.52	15.40	14.17	21.69	24.49	46.18

316

317 **4 Discussion**

318 In this study, we provided the new version of 1-km resolution maps of SOCS across
 319 the Third Pole at 0–300cm depth intervals, and largely makes up for the deficiencies of
 320 previous studies (Ding et al., 2016; Ding et al., 2019; Wang et al., 2020). On the one
 321 hand, our predictions have higher resolution than those studies. Take an example and
 322 focus on a $4.5 \times 10^4 \text{ km}^2$ local area situated in the Budongquan area of Qinghai province,
 323 China (Fig. 8). It can be seen from the excerpts of the map that our prediction is much
 324 more detailed than previous studies. Thus, our predictions better represented spatial
 325 variation of the SOCS across the Third pole region, especially for those regions with
 326 large heterogeneity. On the other hand, these reports most focused on the permafrost
 327 regions rather than the whole Third Pole (Ding et al., 2016; Wang et al., 2020). To date,
 328 few studies have investigated the SOC storage and spatial patterns in areas of seasonally
 329 frozen ground in the Third Pole region. In this study, we created high spatial resolution
 330 data of SOCS distribution in the whole Third Pole by compiling all the field data and
 331 using machine learning methods, thus providing more accurate data than previous
 332 studies.

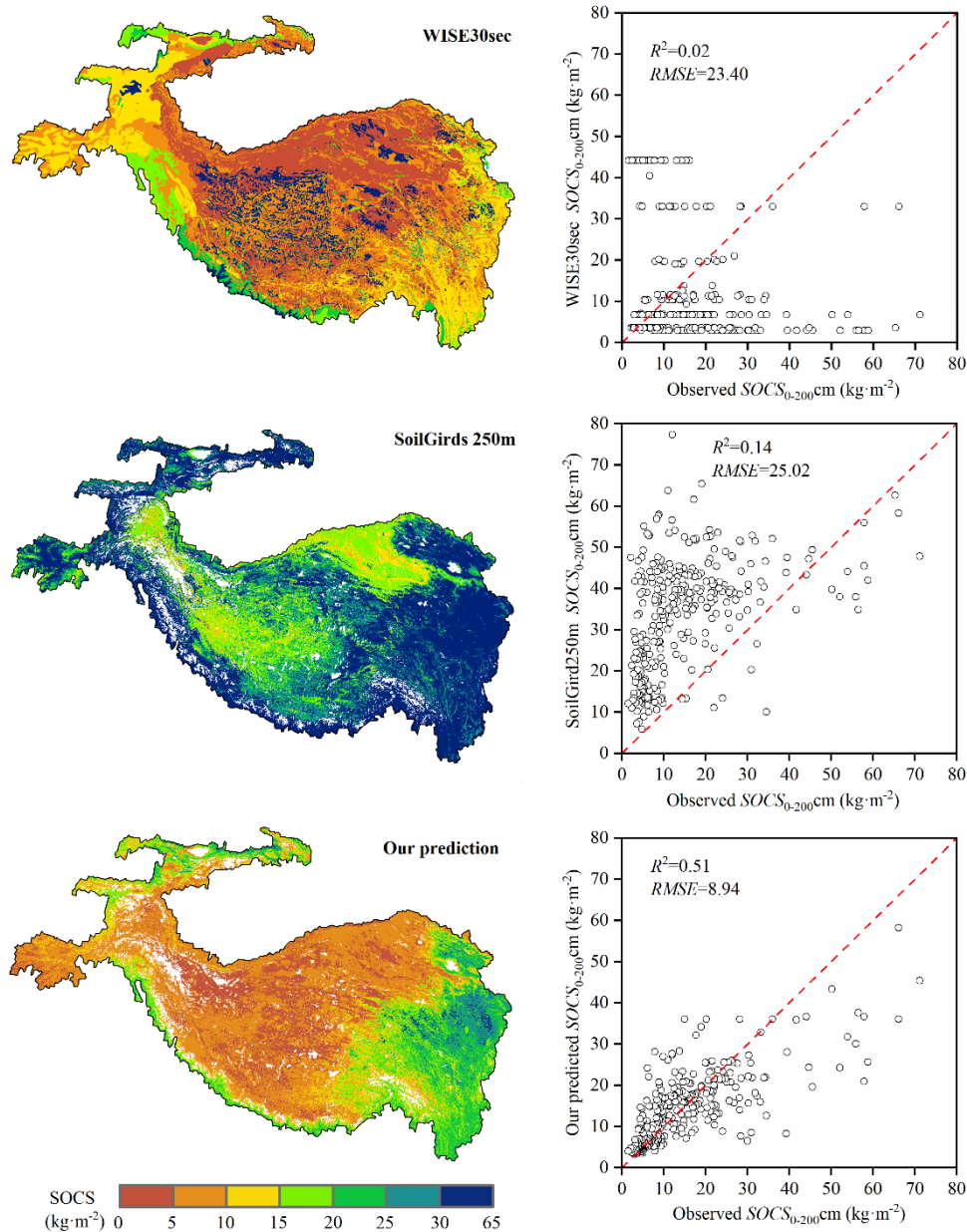


333

334 **Figure 8.** Comparison of spatial details of the predictions with the previous studies: SOCS at 0–
 335 300 cm depth in the map excerpt of Budongquan area of Qinghai province, China. (a) Ding et al.,
 336 2016; (b) Ding et al., 2019; (c) Wang et al., 2020; (d) This study.

337 In addition, our predictions were much more accurate than the existing global SOC
 338 datasets. Figure 9 shows accuracy assessments of our predictions, the SoilGrids250m

339 from Hengl et al., (2017) and the WISE30sec SOCS data from Batjes., (2016) at 0-2m
340 depth intervals based on the 213 SOC stocks data from Ding et al., (2016) and field
341 investigations. We found that our prediction had a higher R^2 value and lower *RMSE*
342 value than SoilGrids250m and WISE30sec. The lowest accuracy was found for the
343 WISE30sec maps, showing the advantage of digital soil mapping based on machine
344 learning over conventional mapping method based on the vegetation/soil units (Liu et
345 al., 2020). The remarkably lower accuracy of SoilGrids250m than our predictions
346 mainly because of serious over-estimation of bulk density, and neglected the influence
347 of coarse gravel content (Hengl et al., 2017). Soil profile data used in SoilGrids250m
348 at Third Pole region are mainly from second China's national soil survey, which lacked
349 accurate information on coarse gravel content and bulk density (Shi et al., 2016). In
350 addition, almost all of these soil profiles are within 1-m depth, which could be a great
351 instability in calculating the deeper SOC by SoilGrids250m. Moreover, the global
352 model building could be less accurate than the regional model building when focusing
353 on a regional extent (Vitharana et al., 2019; Liu et al., 2020). Consequently, our
354 predictions were much more accurate than the existing maps of SOCS.



355

356 **Figure 9.** Comparison of the SOCS prediction with the WISE30sec from Batjes., (2016) and the
 357 SoilGrids250m from Hengl et al., (2017) at 0–200 cm depth intervals based on the 213 SOCS data
 358 from Ding et al., (2016) and field investigations.

359 Our study provides new and more accurate data on SOC storage and spatial patterns
 360 for a depth interval of 0–3 m at a 1 km² scale over the Third Pole region, thus providing
 361 basic data for future studies pertaining to Earth system modeling. We note that a lack
 362 of deep soil pits in forest, shrub, and cropland ecosystems (Fig. S2) means some
 363 uncertainties in the estimation of deep SOC pools remain; however, the collective area
 364 of these ecosystems accounts for < 6% of the total area of the Third Pole region and

365 may have a relatively small influence on total SOC pools (Fig. S1). Regardless, there
366 is a need for large-scale soil surveys that include these areas in order to obtain more
367 accurate information on the SOC storage and distribution in the Third Pole region.
368 Furthermore, regional SOC pools are affected by many other factors, such as soil
369 moisture (Wu et al., 2016) and grazing activities (Zhou et al., 2017), which were not
370 considered in our study due to lack of high-resolution data with a high accuracy. Future
371 work should consider the influence of these factors on SOC at a regional scale to obtain
372 more accurate datasets.

373 **5. Data availability**

374 The datasets of SOC stocks distribution in GeoTiff format are available at
375 <https://doi.org/10.5281/zenodo.4293454> (Wang et al., 2020). The file name is "TP-
376 SOC-d.tif", where d represents soil depth, for example, "TP-SOC-30.tif" represents the
377 spatial distribution of SOC stocks in the Third Pole regions of the upper 30 cm depth
378 interval.

379 **6. Conclusions**

380 This study simulated the spatial pattern of the SOCS over the Third Pole region, and
381 systematically estimated the SOC storage (46.18 Pg) at a depth interval of 0–3 m for
382 the first time. Our results demonstrated that combining multi-environmental factors
383 with machine learning techniques (RF, SVM, and GBRT) can offer an effective and
384 powerful modeling approach for mapping the spatial patterns of SOC. Furthermore, this
385 study provided datasets of SOCS and SOC storage for permafrost and seasonally frozen
386 ground at different soil depths (0–30 cm, 0–50 cm, 0–100 cm, 0–200 cm, and 0–300
387 cm) across the Third Pole region. These datasets can be used to modify existing Earth
388 system models and improve prediction accuracy, and also serve as a reference for
389 policymakers to formulate more effective carbon budget management strategies.

390 **Author contributions**

391 The study was completed with cooperation between all authors. Tonghua Wu and
392 Xiaodong Wu conceived the idea of mapping the spatial distribution of the SOC across
393 the Third Pole regions. Dong Wang conducted the data analyses and wrote the paper.

394 All authors discussed the simulation results and helped revise the paper.

395 **Competing interests**

396 The authors declare that they have no conflict of interest.

397 **Acknowledgements**

398 This work was financially supported by the State Key Laboratory of Cryospheric
399 Science (SKLCS-ZZ-2020), the National Natural Science Foundations of China
400 (41690142, 41721091, 41771076, 41961144021, 41671070), and the CAS "Light of
401 West China" Program.

402 **References**

- 403 Amundson, R.: The Carbon Budget in Soils, *Annual Review of Earth & Planetary Sciences*, 29,
404 535-562, <https://doi.org/10.1146/annurev.earth.29.1.535>, 2001.
- 405 Batjes, N.H.: Harmonized soil property values for broad-scale modelling (WISE30sec) with
406 estimates of global soil carbon stocks. *Geoderma* 269, 61–68,
407 <https://doi.org/10.1016/j.geoderma.2016.01.034>, 2016.
- 408 Cheng, G., Wu, T.: Responses of permafrost to climate change and their environmental
409 significance, Qinghai-Tibet Plateau, *Journal of Geophysical Research Earth Surface*, 112,
410 F02S03, <https://doi.org/10.1029/2006JF000631>, 2007.
- 411 Cheng, G., Zhao L., Li R., Wu, X., Sheng., Y, Hu G., Zou D, Jin, H, Li, X., and Wu., Q.:
412 Characteristic, changes and impacts of permafrost on Qinghai-Tibet Plateau (in Chinese),
413 *Chin Sci Bull*, 64: 2783–2795, <https://doi.org/10.1360/TB-2019-0191>, 2019.
- 414 Ding, J., Li, F., Yang, G., Chen, L., Zhang, B., Liu, L., Fang, K., Qin, S., Chen, Y., Peng, Y., Ji,
415 C., He, H., Smith, P., and Yang, Y.: The permafrost carbon inventory on the Tibetan Plateau:
416 a new evaluation using deep sediment cores, *Global Change Biology*, 22, 2688-2701,
417 <https://doi.org/10.1111/gcb.13257>, 2016.
- 418 Ding, J., Wang, T., Piao, S., Smith, P., and Zhao, L.: The paleoclimatic footprint in the soil
419 carbon stock of the Tibetan permafrost region, *Nature Communications*, 10, 1-9,
420 <https://doi.org/10.1038/s41467-019-12214-5>, 2019.
- 421 Ding, Y., Mu, C., Wu, T., Hu, G., Zou, D., Wang, D., Li, W., and Wu, X.: Increasing cryospheric
422 hazards in a warming climate, *Earth-Science Reviews*, 213,
423 <https://doi.org/10.1016/j.earscirev.2020.103500>, 2021.
- 424 Drake, J. M. and Guisan, R. A.: Modelling Ecological Niches with Support Vector Machines,
425 *Journal of Applied Ecology*, 43, 424-432, <https://doi.org/10.1111/j.1365-2664.2006.01141.x>,
426 2006.
- 427 Elith, J., Leathwick, J. R., and Hastie, T.: A working guide to boosted regression trees, *Journal*
428 *of Animal Ecology*, 77, 802-813, <https://doi.org/10.1111/j.1365-2656.2008.01390.x>, 2008.
- 429 Fan, J., Cao, Y., Yan, Y., Lu, X., Wang, X., Fan, J., Cao, Y., Yan, Y., Lu, X., and Wang, X.:
430 Freezing-thawing cycles effect on the water soluble organic carbon, nitrogen and microbial
431 biomass of alpine grassland soil in Northern Tibet, *African Journal of Microbiology Research*,

432 6, 562-567, <https://doi.org/10.5897/AJMR11.1218>, 2012.

433 Hao, Y., Luo, X., Zhong, B., and Yang, A.: Methods of the National Vegetation Classification
434 based on Vegetation Partition, Remote Sensing Technology and Application, 32, 315-323,
435 <https://doi.org/10.2991/mmme-16.2016.60>, 2017.

436 Hengl T, Mendes de Jesus J, Heuvelink GBM, Ruiperez Gonzalez M, Kilibarda M, Blagotić A,
437 et al.: SoilGrids250m: Global gridded soil information based on machine learning. PLoS
438 ONE 12(2): e0169748. <https://doi.org/10.1371/journal.pone.0169748>, 2017.

439 Hugelius, G., Strauss, J., Zubrzycki, S., Harden, J. W., Schuur, E. A. G., Ping, C. L.,
440 Schirrmeister, L., Grosse, G., Michaelson, G. J., Koven, C. D., O'Donnell, J. A., Elberling,
441 B., Mishra, U., Camill, P., Yu, Z., Palmtag, J., and Kuhry, P.: Estimated stocks of circumpolar
442 permafrost carbon with quantified uncertainty ranges and identified data gaps,
443 Biogeosciences, 11, 6573-6593, <https://doi.org/10.5194/bg-11-6573-2014>, 2014.

444 Jiang, L., Chen, H., Zhu, Q., Yang, Y., Li, M., Peng, C., Zhu, D., and He, Y.: Assessment of
445 frozen ground organic carbon pool on the Qinghai-Tibet Plateau, Journal of Soils and
446 Sediments, 19, 128-139, <https://doi.org/10.1007/s11368-018-2006-3>, 2019.

447 Jobbagy, E. G. and Jackson, R. B.: The vertical distribution of soil organic carbon and its
448 relation to climate and vegetation, Ecological Applications, 10, 423-436,
449 <https://doi.org/10.2307/2641104>, 2000.

450 Koven, C. D., Ringeval, B., Friedlingstein, P., Ciais, P., Cadule, P., Khvorostyanov, D., Krinner,
451 G., and Tarnocai, C.: Permafrost carbon-climate feedbacks accelerate global warming,
452 Proceedings of the National Academy of Sciences, 2011.
453 <https://doi.org/10.1073/pnas.1103910108>, 2011.

454 Li, F., Zang, S., Liu, Y., Li, L., and Ni, H.: Effect of Freezing–Thawing Cycle on Soil Active
455 Organic Carbon Fractions and Enzyme Activities in the Wetland of Sanjiang Plain, Northeast
456 China, Wetlands, 40, 167-177, <https://doi.org/10.1007/s13157-019-01164-9>, 2020.

457 Liang, S., Zhao, X., Liu, S., Yuan, W., Cheng, X., Xiao, Z., Zhang, X., Liu, Q., Cheng, J., Tang,
458 H., Qu, Y., Bo, Y., Qu, Y., Ren, H., Yu, K., and Townshend, J.: A long-term Global Land
459 Surface Satellite (GLASS) dataset for environmental studies, International Journal of Digital
460 Earth, 6, 5-33, <https://doi.org/10.1080/17538947.2013.805262>, 2013.

461 Hengl T, Mendes de Jesus J, Heuvelink GBM, Ruiperez Gonzalez M, Kilibarda M, Blagotić A,

462 et al.: SoilGrids250m: Global gridded soil information based on machine learning. PLoS
463 ONE 12(2): e0169748. <https://doi.org/10.1371/journal.pone.0169748>, 2017.

464 Lombardozzi, D. L., Bonan, G. B., Smith, N. G., Dukes, J. S., and Fisher, R. A.: Temperature
465 acclimation of photosynthesis and respiration: A key uncertainty in the carbon cycle–climate
466 feedback, *Geophysical Research Letters*, 42, 8624-8631,
467 <https://doi.org/10.1002/2015GL065934>, 2016.

468 McGuire, A. D., Lawrence, D. M., Koven, C., Clein, J. S., Burke, E., Chen, G., Jafarov, E.,
469 Macdougall, A. H., Marchenko, S., Nicolsky, D., Peng, S., Rinke, A., Ciais, P., Gouttevin, I.,
470 Hayes, D. J., Ji, D., Krinner, G., Moore, J. C., Romanovsky, V., Schädel, C., Schaefer, K.,
471 Schuur, E. A. G., and Zhuang, Q.: Dependence of the evolution of carbon dynamics in the
472 northern permafrost region on the trajectory of climate change, *Proceedings of the National
473 Academy of Sciences*, 115, 3882-3887, <https://doi.org/10.1073/pnas.1719903115>, 2018.

474 Mishra, U., Jastrow, J. D., Matamala, R., Hugelius, G., Koven, C. D., Harden, J. W., Ping, C.
475 L., Michaelson, G. J., Fan, Z., and Miller, R. M.: Empirical estimates to reduce modeling
476 uncertainties of soil organic carbon in permafrost regions: a review of recent progress and
477 remaining challenges, *Environmental Research Letters*, 8, 1402-1416,
478 <https://doi.org/10.1088/1748-9326/8/3/035020>, 2013.

479 Mu, C. C., Abbott, B. W., Norris, A. J., Mu, M., Fan, C. Y., Chen, X., Jia, L., Yang, R. M.,
480 Zhang, T. J., Wang, K., Peng, X. Q., Wu, Q. B., Guggenberger, G., and Wu, X. D.: The status
481 and stability of permafrost carbon on the Tibetan Plateau, *Earth-Science Reviews*, 211, 21,
482 <https://doi.org/10.1016/j.earscirev.2020.103433>, 2020.

483 Mu, C., Shang, J., Zhang, T., Fan, C., Wang, S., Peng, X., Zhong, W., Zhang, F., Mu, M., and
484 Jia, L.: Acceleration of thaw slump during 1997–2017 in the Qilian Mountains of the northern
485 Qinghai-Tibetan plateau, *Landslides*, 17, 1051-1062, <https://doi.org/10.1007/s10346-020-01344-3>, 2020.

487 Mu, C., Zhang, T., Wu, Q., Peng, X., Cao, B., Zhang, X., Cao, B., and Cheng, G.: Editorial:
488 Organic carbon pools in permafrost regions on the Qinghai–Xizang (Tibetan) Plateau, 9, 479-
489 486, <https://doi.org/10.5194/tc-9-479-2015>, 2015.

490 Obu, J., Westermann, S., Bartsch, A., Berdnikov, N., Christiansen, H. H., Dashtseren, A.,
491 Delaloye, R., Elberling, B., Etzelmüller, B., Kholodov, A., Khomutov, A., Käab, A., Leibman,

492 M. O., Lewkowicz, A. G., Panda, S. K., Romanovsky, V., Way, R. G., Westergaard-Nielsen,
493 A., Wu, T., Yamkhin, J., and Zou, D.: Northern Hemisphere permafrost map based on TTOP
494 modelling for 2000–2016 at 1 km² scale, *Earth-Science Reviews*, 193, 299-316,
495 <https://doi.org/10.1016/j.earscirev.2019.04.023>, 2019.

496 Ping, C. L., Jastrow, J. D., Jorgenson, M. T., Michaelson, G. J., and Shur, Y. L.: Permafrost soils
497 and carbon cycling, *Soil*, 1, 147-171, <https://doi.org/10.5194/soil-1-147-2015>, 2015.

498 Ran, Y., Li, X., and Cheng, G.: Climate warming has led to the degradation of permafrost
499 stability in the past half century over the Qinghai-Tibet Plateau. Copernicus GmbH,
500 <https://doi.org/10.5194/tc-2017-120>, 2017.

501 Schuur, E. A. G., McGuire, A. D., Schädel, C., Grosse, G., Harden, J. W., Hayes, D. J., Hugelius,
502 G., Koven, C. D., Kuhry, P., Lawrence, D. M., Natali, S. M., Olefeldt, D., Romanovsky, V.
503 E., Schaefer, K., Turetsky, M. R., Treat, C. C., and Vonk, J. E.: Climate change and the
504 permafrost carbon feedback, *Nature*, 520, 171-179, <https://doi.org/10.1038/nature14338>,
505 2015.

506 Shi Jianping, Song Ge.: Soil Type Database of China: A nationwide soil dataset based on the
507 Second National Soil Survey (in Chinese). *China Scientific Data*, (2):1-12,
508 <http://dx.doi.org/10.11922/sciencedb.180.88>, 2016.

509 Song, X. D., Brus, D. J., Liu, F., Li, D.-C., Zhao, Y. G., Yang, J. L., and Zhang, G. L.: Mapping
510 soil organic carbon content by geographically weighted regression: A case study in the Heihe
511 River Basin, China, *Geoderma*, 261, 11-22, <https://doi.org/10.1016/j.geoderma.2015.06.024>,
512 2016.

513 Stocker, T. F., Qin, D., Plattner, G. K., Tignor, M., Allen, S. K., Boschung, J., Nauels, A., Xia,
514 Y., Bex, B., and Midgley, B. M.: IPCC, 2013: Climate Change 2013: The Physical Science
515 Basis. Contribution of Working Group I to the Fifth Assessment Report of the
516 Intergovernmental Panel on Climate Change, *Computational Geometry*, 18, 95-123, 2013.

517 Stow, D. A., Hope, A., McGuire, D., Verbyla, D., Gamon, J., Huemmrich, F., Houston, S.,
518 Racine, C., Sturm, M., Tape, K., Hinzman, L., Yoshikawa, K., Tweedie, C., Noyle, B.,
519 Silapaswan, C., Douglas, D., Griffith, B., Jia, G., Epstein, H., Walker, D., Daeschner, S.,
520 Petersen, A., Zhou, L., and Myneni, R.: Remote sensing of vegetation and land-cover change
521 in Arctic Tundra Ecosystems, *Remote Sensing of Environment*, 89, 281-308,

522 <https://doi.org/10.1016/j.rse.2003.10.018>, 2004.

523 Tian, Y., Ouyang, H., Xu, X., Song, M., and Zhou, C.: Distribution characteristics of soil
524 organic carbon storage and density on the Qinghai-Tibet Plateau, *Acta Pedologica Sinica*, 45,
525 933-942, 2008.

526 Tin Kam, H.: Random subspace method for constructing decision forests, *IEEE Transactions*
527 *on Pattern Analysis and Machine Intelligence*, 20, 832-844,
528 <https://doi.org/10.1109/34.709601>, 1998.

529 Turetsky, M. R., Abbott, B. W., Jones, M. C., Walter Anthony, K., Olefeldt, D., Schuur, E. A.
530 G., Koven, C., McGuire, A. D., Grosse, G., Kuhry, P., Hugelius, G., Lawrence, D. M., Gibson,
531 C., and Sannel, A. B. K.: Permafrost collapse is accelerating carbon release, *Nature*, 569, 32-
532 34, <https://doi.org/10.1038/d41586-019-01313-4>, 2019.

533 Vitharana, U., Mishra, U., and Mapa, R. B.: National soil organic carbon estimates can improve
534 global estimates, *Geoderma*, 337, 55-64, <https://doi.org/10.1016/j.geoderma.2018.09.005>,
535 2019.

536 Wang, G., Qian, J., Cheng, G., and Lai, Y.: Soil organic carbon pool of grassland soils on the
537 Qinghai-Tibetan Plateau and its global implication, *Science of the Total Environment*, 291,
538 207-217, [https://doi.org/10.1016/S0048-9697\(01\)01100-7](https://doi.org/10.1016/S0048-9697(01)01100-7), 2002.

539 Wang, T. H., Yang, D. W., Yang, Y. T., Piao, S. L., Li, X., Cheng, G. D., and Fu, B. J.: Permafrost
540 thawing puts the frozen carbon at risk over the Tibetan Plateau, *Science Advances*, 6,
541 <https://doi.org/10.1126/sciadv.aaz3513>, 2020.

542 Wu, Q., Zhang, T., and Liu, Y.: Thermal state of the active layer and permafrost along the
543 Qinghai-Xizang (Tibet) Railway from 2006 to 2010, *The Cryosphere*, 6, 607-612,
544 <https://doi.org/10.5194/tc-6-607-2012>, 2012.

545 Wu, X., Zhao, L., Fang, H., Zhao, Y., Smoak, J. M., Pang, Q., and Ding, Y.: Environmental
546 controls on soil organic carbon and nitrogen stocks in the high-altitude arid western Qinghai-
547 Tibetan Plateau permafrost region, *Journal of Geophysical Research Biogeosciences*, 121,
548 176-187, <https://doi.org/10.1002/2015JG003138>, 2016.

549 Wu, Y., Liu, G., Fu, B., and Guo, Y.: Study on the vertical distribution of soil organic carbon
550 density in the Tibetan Plateau, *Acta Scientiae Circumstantiae*, 28, 362-367,
551 <https://doi.org/10.3724/SP.J.1148.2008.00259>, 2008.

552 Xu, L., Yu, G., and He, N.: Increased soil organic carbon storage in Chinese terrestrial
553 ecosystems from the 1980s to the 2010s, *Journal of Geographical Sciences*, 29, 49-66,
554 <https://doi.org/10.1007/s11442-019-1583-4>, 2019.

555 Yang, Y., Fang, J., Ma, W., Smith, P., Mohammat, A., Wang, S., and Wang, W.: Soil carbon
556 stock and its changes in northern China's grasslands from 1980s to 2000s, *Global Change*
557 *Biology*, 16, 3036-3047, <https://doi.org/10.1111/j.1365-2486.2009.02123.x>, 2010.

558 Yang, Y., Fang, J., Tang, Y., Ji, C., Zheng, C., He, J., and Zhu, B.: Storage, patterns and controls
559 of soil organic carbon in the Tibetan grasslands, *Global Change Biology*, 14, 1592-1599,
560 <https://doi.org/10.1111/j.1365-2486.2008.01591.x>, 2008.

561 Yao, T., Thompson, L. G., Mosbrugger, V., Zhang, F., Ma, Y., Luo, T., Xu, B., Yang, X., Joswiak,
562 D. R., Wang, W., Joswiak, M. E., Devkota, L. P., Tayal, S., Jilani, R., and Fayziev, R.: Third
563 Pole Environment (TPE), *Environmental Development*, 3, 52-64,
564 <https://doi.org/10.1016/j.envdev.2012.04.002>, 2012.

565 Zeng, Y., Feng, Z., Cao, G., and Xu, L.: The Soil Organic Carbon Storage and Its Spatial
566 Distribution of Alpine Grassland in the Source Region of the Yellow River, *Acta Geographica*
567 *Sinica*, 59, 497-504, <https://doi.org/10.1007/BF02873091>, 2004.

568 Zhao, L., Wu, X., Wang, Z., Sheng, Y., Fang, H., Zhao, Y., Hu, G., Li, W., Pang, Q., Shi, J., Mo,
569 B., Wang, Q., Ruan, X., Li, X., and Ding, Y.: Soil organic carbon and total nitrogen pools in
570 permafrost zones of the Qinghai-Tibetan Plateau, *Scientific Reports*, 8,
571 <https://doi.org/10.1038/s41598-018-22024-2>, 2018.

572 Zhou, G., Zhou, X., He, Y., Shao, J., Hu, Z., Liu, R., Zhou, H., and Hosseinibai, S.: Grazing
573 intensity significantly affects belowground carbon and nitrogen cycling in grassland
574 ecosystems: a meta-analysis, *Global Change Biology*, 23, <https://doi.org/1167-1179>,
575 10.1111/gcb.13431, 2017.

576